Desalination and Water Treatment
www.deswater.com
doi: 10.5004/dwt.2022.28162

252 (2022) 361–370
March

Degradation of the azo dye Reactive Black 5 through peroxymonosulfate activation with functional S-doped graphene

Zhong-dong Zhang

Department of Transportation and mechatronics, Xing An Vocational and Technical college, Inner Mongolia Wulanhaote 137400, China, email: 1041928209@qq.com

Received 23 August 2021; Accepted 28 December 2021

ABSTRACT

Peroxymonosulfate (PMS) catalysis based on S-doped graphene (S-GN) is a useful technology for azo dye (Reactive Black 5, RBK5) wastewater treatment. Analyses upon characterization of materials indicated that special S functionalities were introduced into graphene, thereby improving the generation of new surface defects and active sites. In this research, the catalytic degradation of RBK5 by modified materials under different environmental conditions was analyzed. At pH 7 and PMS loading of 3 mmol/L, the degradation efficiency of 10 ppm RBK5 can reach almost 100%, and S-GN showed excellent ion-tolerance performance and cycle stability. The dominant radical species generated through the reaction were identified as $SO_4^{\bullet-}$ and $HO^{\bullet}$ by quenching experiment and electron paramagnetic resonance analysis. Density functional theory calculation was further proposed to determine the activation of PMS with S-GN.

Keywords: Peroxymonosulfate; S-doped graphene; Catalysis; Reactive Black 5

1. Introduction

Industrial advancements are leading to increased disposal of industrial-dye wastewater into urban sewage systems. Dye wastewater has the characteristics of complex composition, high COD, anti-biodegradability, high toxicity, high salt content, high chrominance, and great variation of water quantity [1]. Once discharged into the environment without effective treatment, dye wastewater has serious negative effects on ground water. Azo dyes are typical industrial dye pollutants that are difficult to degrade in the natural environment. After using azo dyes, their disposal without treatment threatens the safety of the water environment. The azo dye Reactive Black 5 (RBK5), which is primarily used in China, is kind of reactive azo dye with azo bond, benzene ring, naphthalene ring, and sulfonic group. The chemical property of RBK5 are stable and difficult to be removed. The traditional sewage-treatment technologies including chemical treatment, physical treatment, and biological treatment are insufficiently effective to degrade RBK5 pollutant [2,3]. Accordingly, advanced oxidation processes (AOPs) based on strong oxidative radicals have been applied to RBK5 dye wastewater treatment.

Among all AOPs, peroxymonosulfate (PMS) exhibits relatively low oxidation potential for pollutant degradation owing to its high bond energy [4]. Thus, PMS oxidation usually requires external activation through physical activation, metal oxide activation, or chemical activation. Physical activation typically includes ultraviolet (UV) irradiation [5] and heating [6,7], activation with metal ions [8] such as Fe^{3+}/Fe^{2+}, Co^{2+}, MnO_2, and Co_3O_4 [9,10], and chemical activation including alkali activation. However, these methods require energy or chemical input and possibly cause metal-ion leaching, in turn resulting in secondary pollution. Thus, the development of an environment-friendly catalytic material to complete PMS activation has become a research hotspot.

The application of carbon-based material to activate PMS has become the trend of environmental application of PMS.

Recently, the PMS catalytic activity of carbon nanotubes, graphite, nano-diamond, 1D single-walled carbon nanotubes, 2D graphene nanosheets, 3D hexagonal ordered mesoporous carbon and cubic ordered mesoporous carbon have been confirmed, consequently [11–13]. For example, Ouyang et al. used pine needles to prepare biochar for the catalytic degradation of 1,4-dioxane with an efficiency of 85% [14]. At present, although the multi-source carbon materials show good catalytic activity for PMS, the complex components of the raw materials lead to the application limitation of poor efficiency and reproducibility, and it is difficult to study the mechanism of PMS activation.

Graphene, as a typical kind of carbon material, is a two-dimensional (2D) honeycomb of six-membered carbon rings that can also warp into a zero-dimensional fullerene, rolled up in one-dimensional carbon nanotubes (CNTs), or stacked into three-dimensional graphite. Graphene-based materials have unique properties including charge transfer, conductivity, mechanical strength, optical properties, and porosity. Different defect sites and functional groups on graphene enable PMS to be catalyzed by breaking the O–O bond, resulting in the generation of different active free radicals [such as $SO_4^{\bullet-}$ and $HO^{\bullet}$ in Eqs. (1)–(6)] [15–18]. In literature, edge defects on the graphene surface are found to be more active than those on the carbon plane. $^1O_2$, as one of the active species, can also be directly generated by edge groups such as C=O group [Eqs. (7)–(9)] [19] or can as a secondary product of free radicals [Eqs. (10)–(13)] [20,21].

$$HSO_5^- + C \rightarrow HO^- + SO_4^{\bullet-} + C^+ \quad (1)$$

$$HSO_5^- + C \rightarrow HO^{\bullet} + SO_4^{2-} + C^+ \quad (2)$$

$$HSO_5^- + C \rightarrow H^+ + SO_5^{\bullet-} + C \quad (3)$$

$$SO_4^{\bullet-} + H_2O \rightarrow H^+ + HO^{\bullet} + SO_4^{2-} \quad (4)$$

$$C{=}C{=}O + HSO_5^- \rightarrow SO_4^{\bullet-} + C{=}C{-}O^+ + OH^- \quad (5)$$

$$C{=}C{-}O^+ + HSO_5^- \rightarrow SO_5^{\bullet-} + C{=}C{=}O + H^+ \quad (6)$$

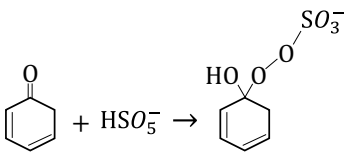

(7)

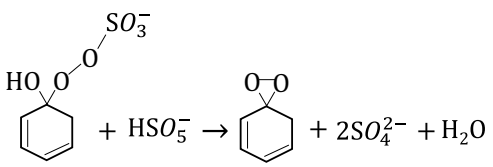

(8)

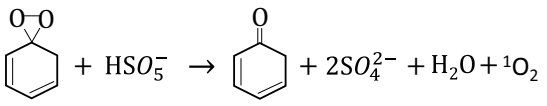

(9)

$$SO_5^{\bullet-} + H_2O \rightarrow HSO_4^- + 1.5^1O_2 \quad (10)$$

$$SO_4^{\bullet-} + HSO_5^- \rightarrow H^+ + {}^1O_2 + SO_4^{2-} \quad (11)$$

$$O_2 + e^- \rightarrow O_2^{\bullet-} \quad (12)$$

$$O_2^{\bullet-} + 2H_2O \rightarrow {}^1O_2 + H_2O_2 + 2OH^- \quad (13)$$

Based on the high catalytic activity of edge defects, increasing the kind and number of edge defects on the graphene surface can enhance the catalytic activity of graphene for PMS activation. As a common technical method of controlling the microstructure of graphene materials, the doping of heteroatoms into graphene theoretically creates more defects in the graphene structure. Among all heteroatoms, the doping of sulfur in the structure of graphene is dominated by edge loading. Given the large difference in bond lengths between C–S (1.78 Å) and C–C (1.42 Å), the sulfur atoms in the sulfur edge load have a height difference of 1.1 Å between the carbon atoms in the plane [22,23], resulting in the hybridization of nonplanar structures. Zhao et al. [24] used thiourea as the precursor of sulfur to prepare sulfur-doped graphene (S-GN)/CNTs (NS-GR/CNT) by hydrothermal method for hydrogen evolution reaction and confirmed that sulfur structure plays an important role in the catalytic reaction. Moreover, the hybridization of the orbitals of S and C atoms results in the inhomogeneous spin-density distribution on S-GN, which reduces the energy difference between the highest occupied molecular orbitals and the lowest unoccupied molecular orbitals of graphene materials [25]. Thus, the doping of S structure can positively enhance the ability of PMS activation and induce the formation of $^1O_2$ [Eq. (14)] [26].

$$C - 2SO_3 - O - OH^- \rightarrow \cdots \rightarrow C + {}^1O_2 + 2H^+ + 2SO_4^{2-} \quad (14)$$

The present study aimed to deepen the discussion on S-GN for PMS activation. Graphene oxide (GO) was selected as the carbon-based raw material to explore the synthesis of S-GN materials by using H_2SO_4 as S precursor. S-doped materials were analyzed under different conditions for the catalytic PMS degradation of RBK5 pollution. The S hybrid structure and catalyst activity was investigated, and the main active species produced were analyzed. Based on the experimental analysis and density functional theory (DFT) theoretical calculation, the possible mechanisms of PMS were clarified. In summary, according to the catalytic efficiency, active species characterization, and DFT calculation, the final results of this research could provide the underlying mechanism of action, as well as the impact of environmental factors on the system, to understand the regularity and process optimization.

2. Materials and methods

2.1. Graphene oxide (GO) preparation

GO preparation can be divided into four stages. First, placed 1.5 g of graphite powder and 1.5 g of sodium nitrate

in a flask and continuously stirred them at 5°C after pouring 60 mL of H_2SO_4 into the flask, 9 g of $KMnO_4$ was slowly added, and the reaction temperature was kept for 30 min. Second, the temperature was raised to 50°C and deionized (DI) water was added dropwise into the flask for 30 min. Third, the solution temperature was raised to 95°C and the temperature was maintained under continuous stirring for 30 min. Fourth and last, the reaction was stopped by adding 100 mL of H_2O_2 solution into the mixture and the final GO was obtained by drying for 24 h at 60°C.

2.2. S-GN preparation

S-GN was prepared by one-step hydrothermal method. GO (0.5 g) was first mixed with 20 mL of H_2SO_4 in 200 mL of DI water and treated with ultrasound in an ice-water bath for 10 min. The mixture was then transferred into a polytetrafluoroethylene autoclave and placed in an oven at 200°C for 6 h of hydrothermal treatment. Afterwards, the samples were washed with DI water and dried to obtain S-GN. The material obtained by the same step without H_2SO_4 addition was marked as graphene (GN).

2.3. Characterization

Crystal morphology and thickness were observed by transmission electron microscopy (TEM; JEOL-2100F) and atomic force microscopy (AFM). Fourier-transform infrared spectroscopy (FTIR; Nicolet iS50 Spectrometer, Thermo Scientific) was conducted to record the surface functional groups. X-ray diffraction (XRD; X'Pert PRO) analysis was performed to investigate the crystal phases of materials. X-ray photoelectron spectroscopy (XPS; ESCALAB250Xi PHI Quantera) was carried out to examine the elements and species of S-GN. Reactive radicals generated during reaction were identified through electron paramagnetic resonance (EPR; JES-FA200) technique.

2.4. RBK5 degradation and detection

About 10 mg/L RBK5 solution was prepared with DI water, and the solution pH was adjusted with NaOH and HCl (5 mmol/L) in a 250 mL beaker. The reaction was initiated by adding some PMS and catalyst. During reaction, whole reaction is kept out of light to eliminate the interference of natural light. All samples were collected at room temperature and filtered through a 0.02 μm-thick membrane. The residual RBK5 concentration was measured with a TU-UV–visible photometer. The maximum absorption wavelength was 600 nm.

2.5. DFT calculations

First-principle calculations of density functional theory were performed using the Cambridge Sequential Total Energy Package. The exchange-correlation function was calculated under the generalized gradient approximation with ultrasoft pseudopotentials and Perdew–Burke–Ernzerhof function. The energy cut-off was set to 280 eV, and gamma *k*-point sampling was tested for convergence. Specifically, the energy tolerance was 5.0×10^{-7} eV per atom and the maximum displacement was 5.0×10^{-4} Å. All calculations referred to the Grimme method for DFT-D correction.

3. Results and discussion

3.1. Characterization

3.1.1. Transmission electron microscopy and atomic force microscopy

In this research, pure GN and S-GN catalysts were prepared by hydrothermal method. The structural morphology of GN and S-GN catalyst was analyzed by TEM. As shown in Fig. 1a and b, GN and S-GN catalysts exhibited a typical 2D disordered and folded sheet-like edges of graphene. Literature shows that a disordered, folded structure exposes high-density active sites, benefiting the catalytic-activity improvement.

AFM was further used to confirm the exfoliation degree of S-GN, and results are shown in Fig. 1c. In accordance with TEM, the S-GN thickness was 0.5–1.5 nm. Given that the single-layer thickness of graphene is 0.34 nm, S-GN more likely had four to five stacked layers.

3.1.2. Fourier-transform infrared spectroscopy

To identify the presence of functional groups on S-GN surface, FTIR spectra were obtained, as shown in Fig. 2a. Peaks located at 3,230 cm^{-1} indicated the O–H stretching vibration of surface-adsorbed water. The responses of C–C, C=O, and C–O were located at around 1,620; 1,720 and 1,040 cm^{-1}, respectively [27,28]. The vibration peaks of C=O and C–O indicated residual oxygen-containing groups on S-GN surface [29]. The appearance of a vibration peak at 1,245 cm^{-1}, related to S=O [30], proved the sulfonation of graphene.

3.1.3. X-ray diffraction

To investigate the effect of S doping on the crystal phases of graphene, XRD was analyzed from 20° to 80°. Fig. 2b shows obvious hexagonal C diffraction peaks at 25.5° without S loading [31]. The obvious peak at 25.5° corresponded to the (002) peak of graphene (JCPDS Card No. 75-1621), whereas with S loading, the hexagonal C structure was broken based on the diminishment of the (002) peak.

3.1.4. X-ray photoelectron spectroscopy

To further prove the functional groups of S-GN surface, detailed information was obtained by XPS spectroscopy. Results from Fig. 3a–c suggested C, S, and O were the main components of S-GN. In Fig. 3a, the typical deconvoluted peaks in the C1s spectrum at 284.5, 286.8, and 291 eV referred to the C–C and C–O/C=O bonds and π–π* bonding in graphene. The appearance of π-π* bonding indicated the aromatic or unsaturated structure of graphene, which was possible related to its sulfonation [32]. In Fig. 3b, the S 2p peak at around 167.5 eV confirmed the sulfonation of graphene as C–SO_x–C species [33]. In accordance with the FTIR results, the existence of oxygen-containing groups on S-GN surface was further proved by an obvious peak at the O1s spectrum in Fig. 3c. The peak located at 533.0 eV indicated the existence of C–O bond [34].

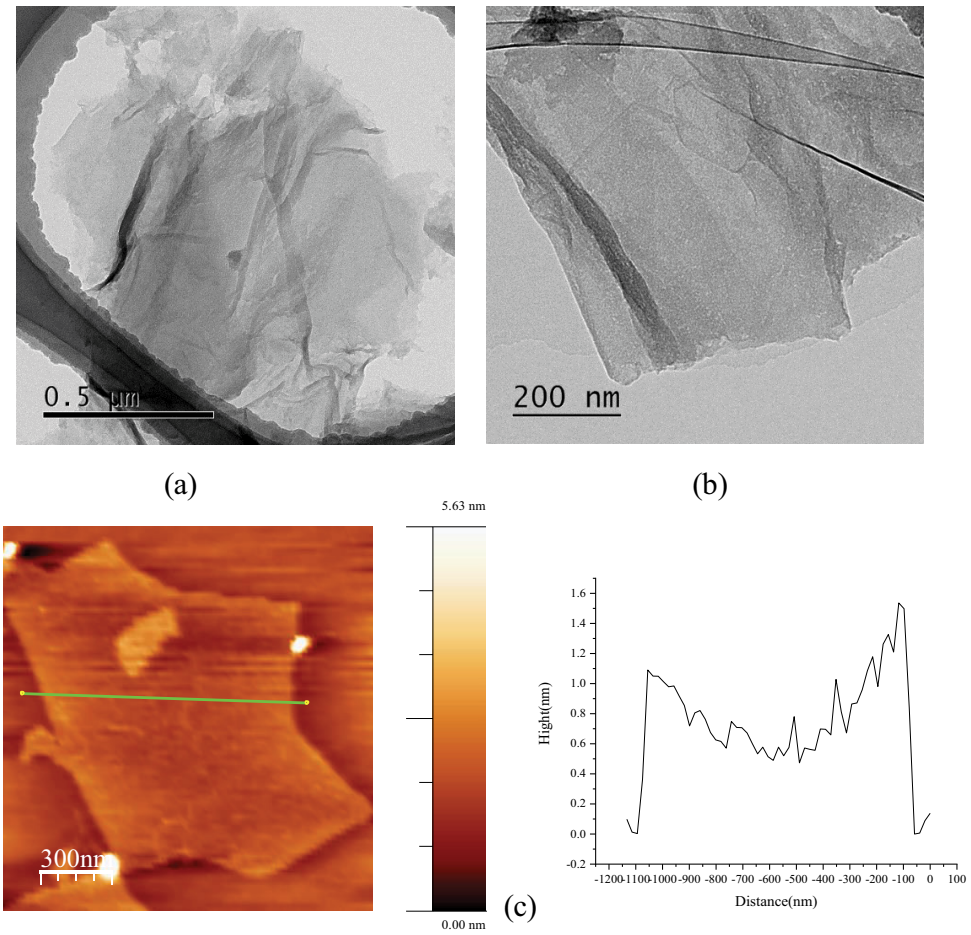

Fig. 1. TEM images of GN (a), S-GN (b) and AFM images of S-GN (c).

3.2. Performance of S-GN for RBK5 degradation

3.2.1. Comparison of different systems

The catalytic activity of S-GN was demonstrated by comparing the degradation efficiency of RBK5 in different systems. Four systems, namely, PMS, S-GN, GN/PMS, and S-GN/PMS, were discussed. The degradation efficiencies of each system are shown in Fig. 4a. In each system, PMS concentration was 3 mmol/L, catalyst dosage was 0.3 g/L, and pH was 7. When S-GN was added alone, RBK5 concentration was almost unchanged, indicating that the catalyst had no adsorption to RBK5. When PMS was alone, the removal rate of RBK5 was 43%. This finding may be due to the fact that PMS is a strong oxidant and RBK5 is highly reductive, and PMS may react directly with RBK5. Results showed that PMS alone could oxidize some RBK5, but the effect was limited. The removal rate of RBK5 was negligible after 90 min of adsorption. S-GN can effectively promote PMS to oxidize RBK5, and the removal rate of RBK5 can reach 100%, higher than the efficiency of the GN/PMS system. Results showed that S-GN could accelerate RBK5 degradation and increase the reaction efficiency of PMS.

To describe the heterogeneous catalytic reaction, Langmuir-Hinshelwood (L-H) kinetics was calculated by Eq. (15). Due to the negligible adsorption of S-GN, the L-H kinetics were further expressed by first order kinetics as Eq. (16).

$$r = -\frac{dC}{dt} = \frac{k_r KC}{1 + KC} \tag{15}$$

where k_r: the reaction rate constant (mol/dm/min); K: adsorption coefficient of the reactant on catalyst (1/mol/dm^3); C: the concentration of the solute (mg/L).

$$-\ln\left(\frac{C}{C_0}\right) = kt \tag{16}$$

where k: the reaction rate constant (equal to $k_r K$, 1/min).

The calculation results were shown in insert figure of Fig. 4a and the reaction rate constant of S-GN (0.056/min) was almost 2 times higher than GN (0.029/min). This results also indicated the superior improvement of catalytic activity with S doping.

3.2.2. Efficiency under various initial pH

To investigate the effect of initial pH on the degradation efficiency of RBK5, the removal efficiency from pH 3 to 11

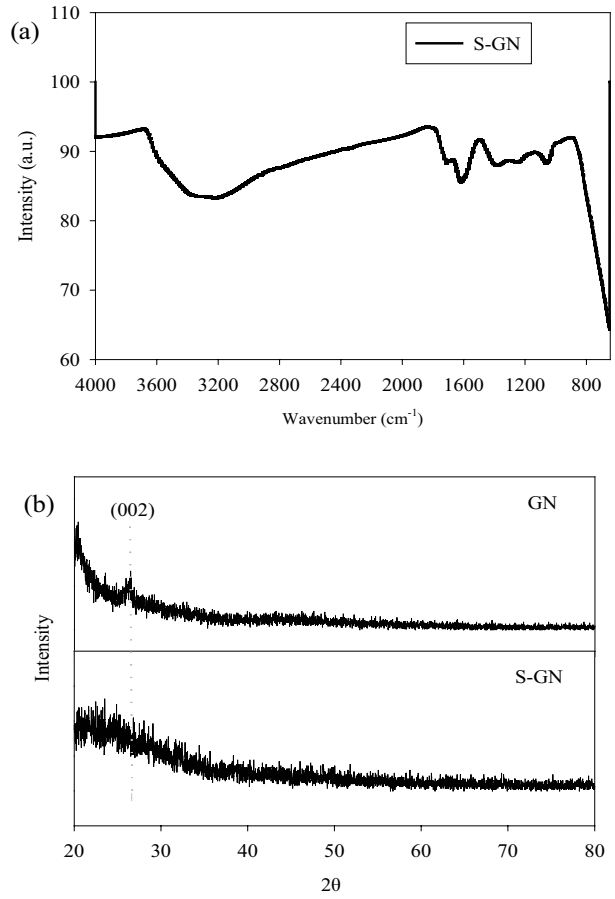

Fig. 2. (a) FTIR spectra of S-GN and (b) XRD patterns of GN and S-GN.

was studied, and results are shown in Fig. 4b. Degradation efficiencies increased with increased pH from 3 to 7. With further increased initial pH to 11, the removal efficiency of RBK5 decreased. For this phenomenon, H^+ in acid condition can inhibit the dissociation of HSO_5^-, and some H_2SO_5 instead of HSO_5^- is generated [35]. H^+ also reacts with $SO_4^{\bullet-}$ and $HO^\bullet$ radicals [Eqs. (17)–(19)], also reducing the degradation effect [36]. Under an alkaline condition, PMS exist as $SO_5^{\bullet-}$ ion because the pK_a of PMS is 9.4, resulting in reduced radical generation [37]. However, the removal rate of RBK5 was above 85% under the initial conditions of acid, neutral, and alkaline conditions, indicating that the system maintained high catalytic activity within various pH ranges.

$$HSO_5^- \rightarrow SO_5^{2-} + H^+ \quad (17)$$

$$H^+ + SO_4^{\bullet-} + e^- \rightarrow HSO_4^- \quad (18)$$

$$H^+ + HO^\bullet + e^- \rightarrow H_2O \quad (19)$$

3.2.3. Effect of PMS loading

The effects of PMS dosages of 1, 3, and 5 mmol/L on RBK5 removal were investigated. The results are as shown

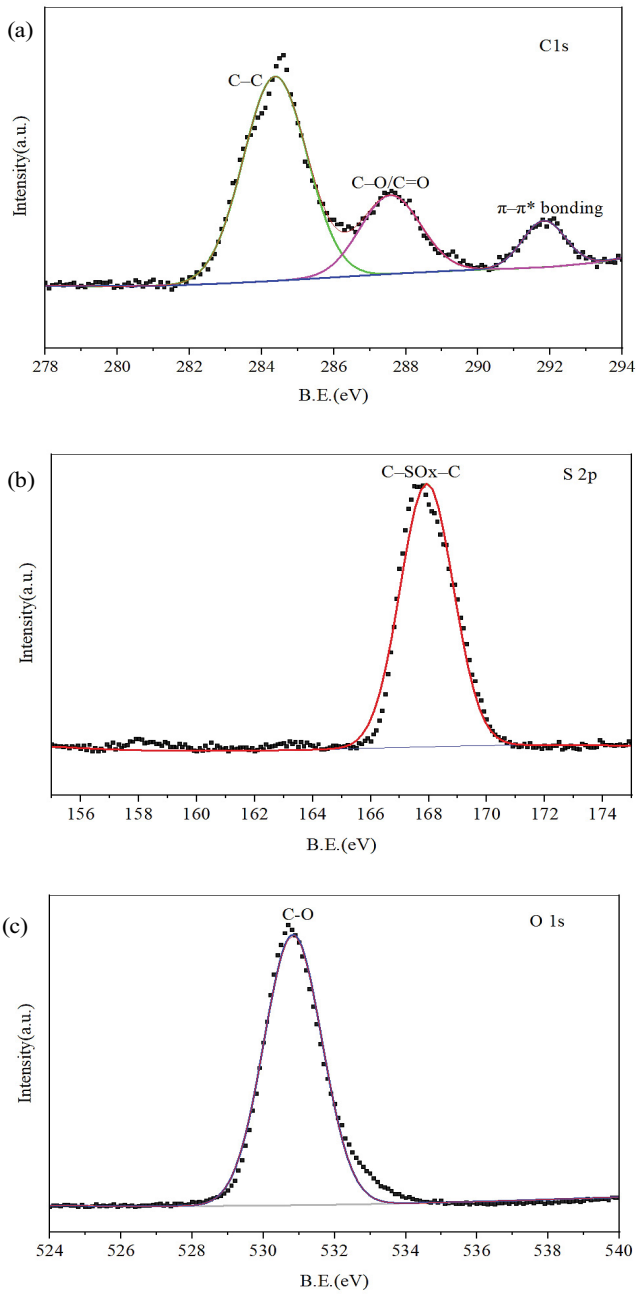

Fig. 3. XPS spectra of S-GN, (a) C1s images, (b) S2p images, and (c) O1s images.

in Fig. 4c. When the dosage of PMS was 1 mmol/L, the removal rate of RBK5 was 88%. With increased PMS dosage to 3 mmol/L, it was 92% in 60 min. With further increased PMS dosage to 5 mmol/L, almost no change occurred in the removal efficiency of RBK5 in 60 min. With increased PMS dosage, the removal efficiency and degradation efficiency initially accelerated and then decreased. This finding was due to S-GN providing a limited number of active catalytic sites. When the PMS concentration was excessive, a quenching reaction occurred between the free radicals, and the sulfate radical reacted with the hydrogen persulfate ion to

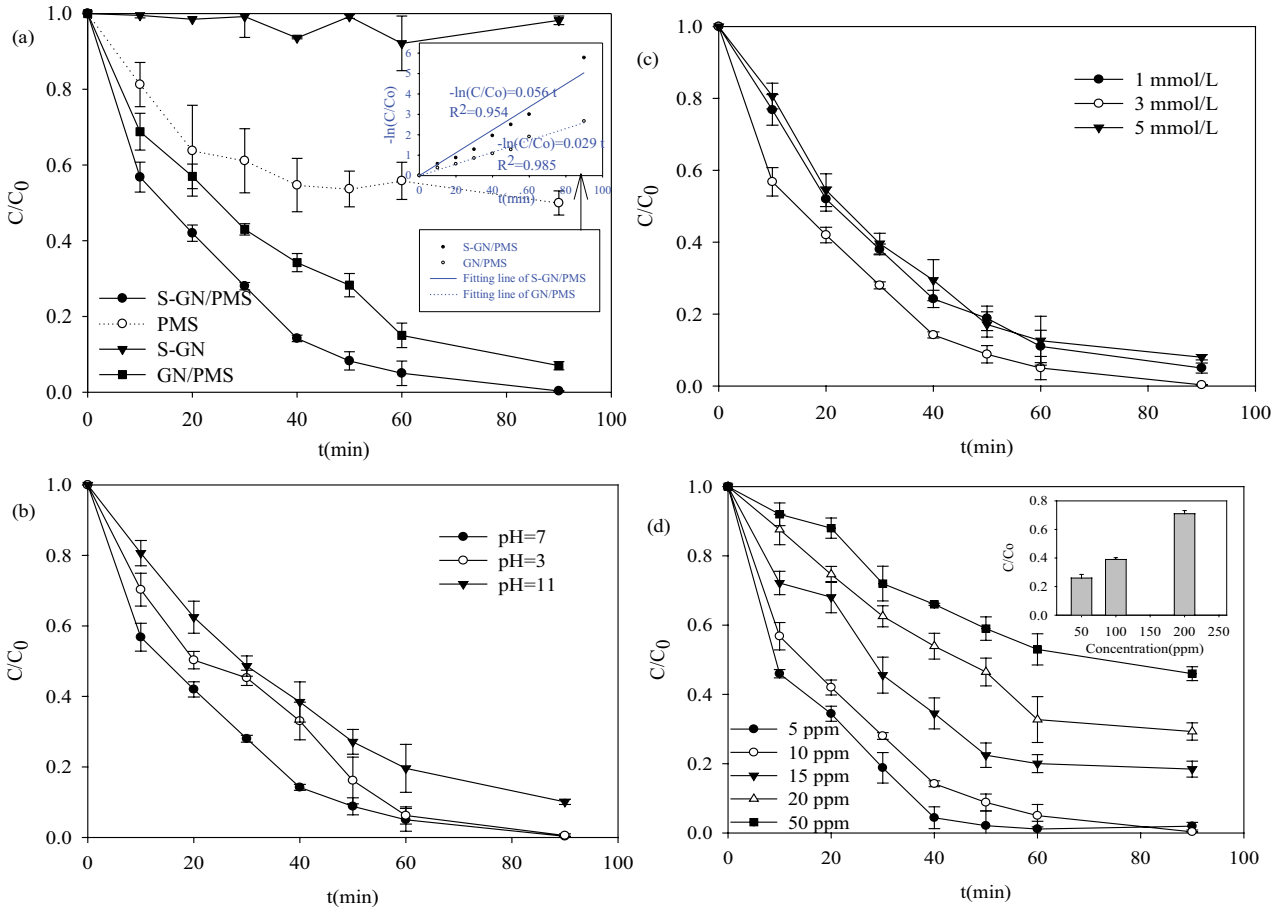

Fig. 4. (a) RBK5 degradation under various systems (insert figure shown the calculation results of first-order kinetics), (b) RBK5 degradation under various initial pH, (c) RBK5 degradation under various PMS loading, (d) RBK5 degradation under various RBK5 concentration (insert figure shown the RBK5 degradation under various RBK5 concentration under 6 mmol/L PMS within 180 min).

produce $SO_5^{\bullet-}$ [38]. $SO_5^{\bullet-}$ has weak oxidation ability, as shown in Eqs. (20) and (21).

$$SO_4^{\bullet-} + SO_4^{\bullet-} \rightarrow S_2O_8^{2-} \quad (20)$$

$$SO_4^{\bullet-} + HSO_5^- \rightarrow SO_5^{\bullet-} + SO_4^{2-} + H^+ \quad (21)$$

3.2.4. Effect of RBK5 concentration

Under the conditions of pH 7 and [PMS] = 3 mmol/L, the degradation effect of the dye at the concentrations of 5, 10, 15, and 20 ppm was determined, and results are shown in Fig. 4d. The degradation efficiency of the dye gradually decreased with increased dye concentration. When the dye concentration was 5, 10, 15, and 20 ppm, the degradation efficiency was 100%, 100%, 80%, and 73%, respectively. Further increase the RBK5 concentration to 50 ppm, the degradation efficiency was maintained around 50%. Owing to the increase in substrate concentration, the free radicals generated were limited, saturating the utilization of free radicals. The resulting intermediate competed with the substrate for free radicals, thereby reducing the removal efficiency of the substrate [39]. To test the application possibility under high concentration, 50–200 ppm RBK5 solution was also analyzed under pH 7 and [PMS] = 6 mmol/L as shown in insert figure of Fig. 4d. The results indicated high concentration wastewater can be effectively degraded by increasing the dosage of PMS within 180 min.

3.2.5. Interference of ions

Owing to the salt auxiliary content of actual dye wastewater, 10 mmol/L NaCl, Na_2CO_3, and $NaNO_3$ were added to the reaction system to investigate the effect of salt ions on the removal rate of RBK5. As shown in Fig. 5a, the removal rate of RBK5 was 100% at 90 min without salt ions, and 98%, 91%, and 59% at 30 min with NaCl, $NaNO_3$, and Na_2CO_3, respectively. Obviously, all ions inhibited the degradation of RBK5 in the S-GN/PMS system. Salt ions competed with PMS for the active site of the catalyst, thereby degrading the catalyst activity.

3.2.6. Effect of recycle times

Recycle times, which is a critical factor that determines whether a material can be subjected to further utilization,

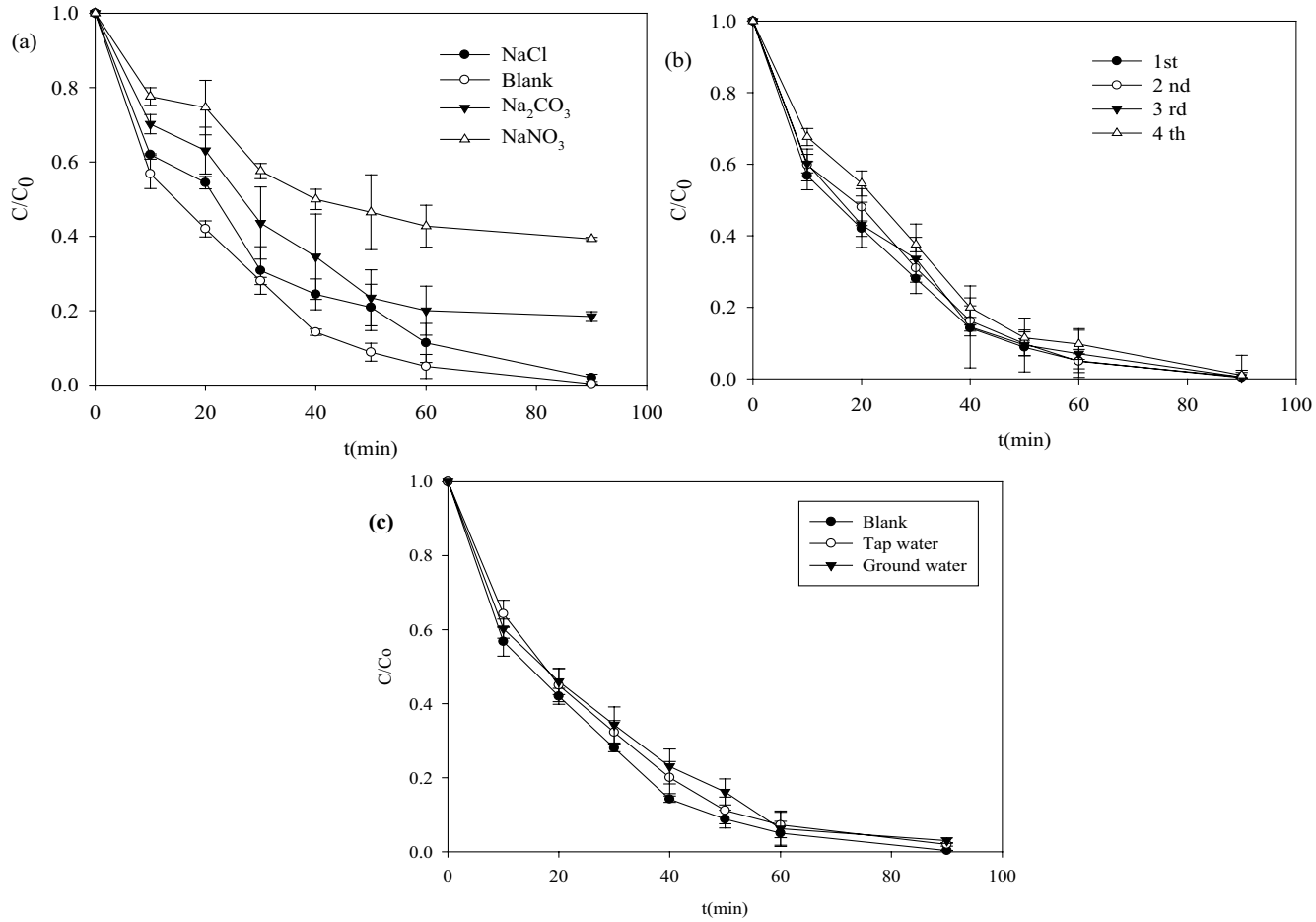

Fig. 5. (a) RBK5 degradation under various interference of ions, (b) RBK5 degradation with recycled S-GN, and (c) RBK5 degradation under various actual water source.

was investigated to verify the long-term stability of the catalyst. For each new cycle, S-GN was collected and vacuum dried at room temperature overnight. As shown in Fig. 5b, with increased recycle number, the efficiency of S-GN remained stable. After three cycles, the stabilized efficiency confirmed that S-GN can be reused.

3.2.7. Application in actual water

To evaluate the utilization potentiality of the catalyst, its application in actual water was analyzed as shown in Fig. 5c. In the actual water source of tap water and ground water (landscape water of reuse water), similar RBK5 degradation efficiency can be achieved, indicated the strong resistance of the catalyst to water source [40]. The results of application in actual water further proved that the PMS activation system via functional S-doped graphene is doable for the treatment of actual wastewater.

3.2.8. Radicals generation

RBK5 degradation was quenched by methanol and tert-butanol to determine the kinds of free radicals produced in the system. Methanol is the scavenger of the free radicals $SO_4^{\bullet-}$ ($k = 2.5 \times 10^7\ M^{-1}\ s^{-1}$) and $HO^{\bullet}$ ($k = 9.7 \times 10^8\ M^{-1}\ s^{-1}$), and tert-butanol is the scavenger of $HO^{\bullet}$ ($k = 3.8\sim7.6 \times 10^8\ M^{-1}\ s^{-1}$), rather than $SO_4^{\bullet-}$ ($k = 4.0\sim9.1 \times 10^5\ M^{-1}\ s^{-1}$) [41]. In addition, to determine the influence of non-radical pathways at the same time, L-histidine were used to capture the $^1O_2$ [42]. All the quenching reaction was carried out with 50 vol% methanol, tert-butanol and L-histidine solution, respectively. As shown in Fig. 6a, about 19%, 38% and 23% efficiency were inhibited by L-histidine, methanol and tert-butanol compared with the blank experiment. This finding suggested that $SO_4^{\bullet-}$ may be the major functional radical compared with $HO^{\bullet}$ because $HO^{\bullet}$ was the secondary product of $SO_4^{\bullet-}$ [Eq. (4)]. The non-radical pathway triggered by $^1O_2$ also contributed to the degradation efficiency of RBK5. To confirm the results of quenching experiment, 5,5-dimethyl-1-pyrroline-1-oxide (DMPO) was used as the scavenger for EPR analysis. As shown in Fig. 6b, slight peak signals were detected with singlet PMS addition, and strong peak signals of $DMPO^{\bullet}$-SO_4^{-} were detected in S-GN/PMS. This phenomenon confirmed the significant role of $SO_4^{\bullet-}$ [43].

3.2.9. DFT calculation

Considering the activation of PMS and S-GN, the interaction between PMS and S-GN was established, as shown in Fig. 7, the partial density of states (PDOS) and adsorption

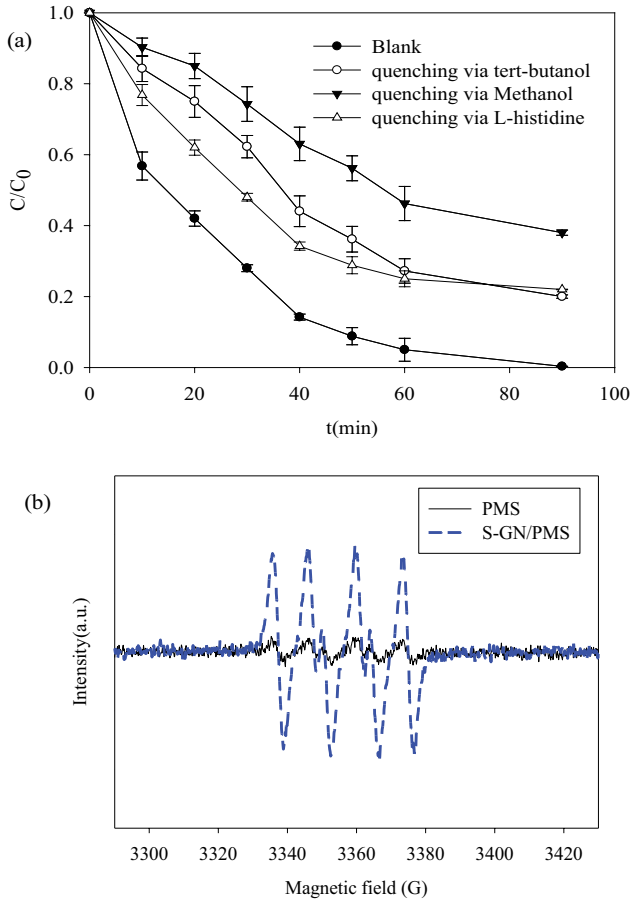

Fig. 6. (a) Quenching experiment and (b) EPR analysis of active species generation.

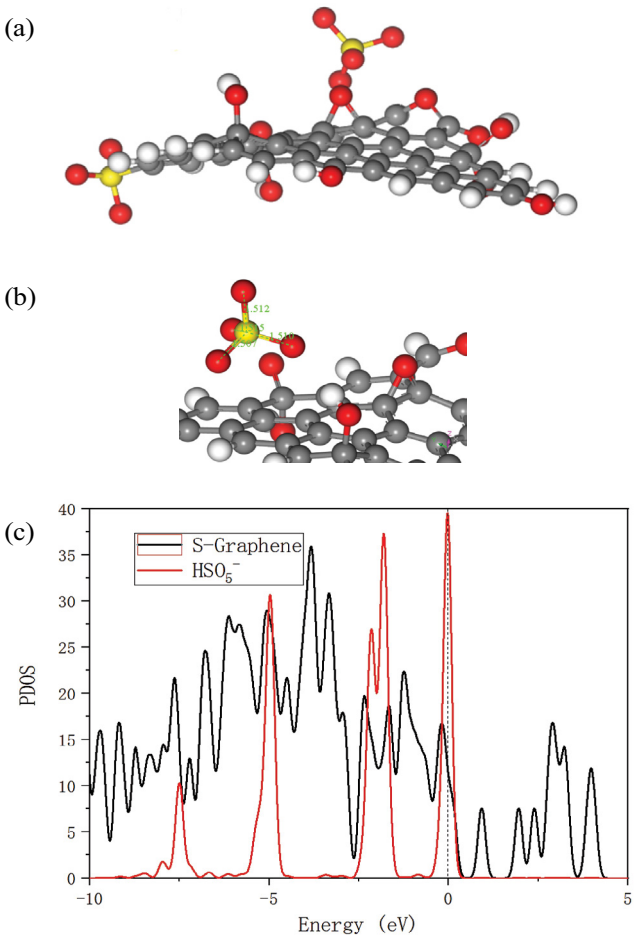

Fig. 7. (a) The interaction model of PMS and S-GN, (b) $SO_4^{\bullet-}$ generation on the surface of S-GN, and (c) PDOS results of PMS and S-GN.

energy were analyzed. Results showed that the adsorption energy of HSO_5^- was −2.647 eV, confirming that S-GN was favorable for PMS attachment to trigger further reactions for $SO_4^{\bullet-}$ generation (Fig. 7a and b). The activation of PMS via S-GN was also proved by PDOS calculation (Fig. 7c) due to the hybridization of PMS and S-GN at the Fermi level (0 eV) [44,45].

4. Conclusion

S-GN was used as a catalyst, and the effect of S doping on RBK5 degradation was investigated. According to the characterization results of S functionalities, C–SO_x–C species was successfully introduced into the graphene structure, thereby inducing surface defects and active sites for PMS activation. Under various conditions of pH, RBK5 concentration, and PMS loading, almost 100% degradation efficiency can be achieved. S-GN also showed superior PMS activity, ion tolerance, and recyclability. Quenching experiments and EPR analysis indicated that $SO_4^{\bullet-}$ was the main active product, and DFT calculation confirmed the breakage of the O–O bond in PMS for $SO_4^{\bullet-}$ generation. In summary, this research provided a simple method of S-GN preparation, analyzed the practical application feasibility of the S-GN/PMS system for azo dye pollution degradation, and further discussed the mechanism underlying PMS activation.

Conflicts of interest

I declare that i have no financial and personal relationships with other people or organizations that can inappropriately influence our work, there is no professional or other personal interest of any nature or kind in any product, service and/or company that could be construed as influencing the position presented in, or the review of, the manuscript entitled, “Degradation of the azo dye Reactive Black 5 through peroxymonosulfate activation with functional S-doped graphene”.

References

[1] H. Safardoust-Hojaghan, M. Salavati-Niasari, Degradation of methylene blue as a pollutant with N-doped graphene quantum dot/titanium dioxide nanocomposite, J. Cleaner Prod., 148 (2017) 31–36.
[2] M.M. Ghoneim, H.S. El-Dosky, N.M. Zidan, Electro-Fenton oxidation of Sunset Yellow FCF azo-dye in aqueous solutions, Desalination, 274 (2011) 22–30.
[3] H. Li, Z. Xiong, X. Dai, Q. Zeng, The effect of perspiration on photo-induced chemical reaction of azo dyes and the determination of aromatic amine products, Dyes Pigm., 94 (2012) 55–59.

[4] J. Wu, L. Ma, Y. Chen, Y. Cheng, Y. Liu, X. Zha, Catalytic ozonation of organic pollutants from bio-treated dyeing and finishing wastewater using recycled waste iron shavings as a catalyst: removal and pathways, Water Res., 92 (2016) 140–148.
[5] G. Zhou, H. Sun, S. Wang, H. Ming Ang, M.O. Tadé, Titanate supported cobalt catalysts for photochemical oxidation of phenol under visible light irradiations, Sep. Purif. Technol., 80 (2011) 626–634.
[6] C. Tan, N. Gao, D. Yang, A. Na, D. Jing, Heat-activated persulfate oxidation of diuron in water, Chem. Eng. J., 203 (2012) 294–300.
[7] C. Tan, N. Gao, Y. Deng, W. Rong, S. Zhou, N. Lu, Degradation of antipyrine by heat activated persulfate, Sep. Purif. Technol., 109 (2013) 122–128.
[8] P. Shukla, H. Sun, S. Wang, H.M. Ang, M.O. Tadé, Nanosized Co_3O_4/SiO_2, for heterogeneous oxidation of phenolic contaminants in waste water, Sep. Purif. Technol., 77 (2011) 230–236.
[9] L. Lai, P. Zhou, H. Zhou, Mi. Sun, Y. Yu, Y. Liu, G. Yao, B. Lai, Heterogeneous Fe(III)/Fe(II) circulation in $FeVO_4$ by coupling with dithionite towards long-lasting peroxymonosulfate activation: pivotal role of vanadium as electron shuttles, Appl. Catal., B, 297 (2021) 120470, doi: 10.1016/j.apcatb.2021.120470.
[10] H. Liang, H. Sun, A. Patel, P. Shukla, Z.H. Zhu, S. Wang, Excellent performance of mesoporous Co_3O_4/SiO_2, nanoparticles in heterogeneous activation of peroxymonosulfate for phenol degradation in aqueous solutions, Appl. Catal., B, 127 (2012) 330–335.
[11] X. Duan, Z. Ao, D. Li, H. Sun, L. Zhou, A. Suvorova, M. Saunders, G. Wang, S. Wang, Surface-tailored nanodiamonds as excellent metal-free catalysts for organic oxidation, Carbon, 103 (2016) 404–411.
[12] S. Indrawirawan, H. Sun, X. Duan, S. Wang, Nanocarbons in different structural dimensions (0–3D) for phenol adsorption and metal-free catalytic oxidation, Appl. Catal., B, 179 (2015) 352–362.
[13] P. Sun, H. Liu, M. Feng, L. Guo, Z. Zhai, Y. Fang, X. Zhang, V.K. Sharma, Nitrogen-sulfur co-doped industrial graphene as an efficient peroxymonosulfate activator: singlet oxygen-dominated catalytic degradation of organic contaminants, Appl. Catal., B, 251 (2019) 335–345.
[14] D. Ouyang, Y. Chen, J. Yan, L. Qian, L. Han, M. Chen, Activation mechanism of peroxymonosulfate by biochar for catalytic degradation of 1,4-dioxane: important role of biochar defect structures, Chem. Eng. J., 370 (2019) 614–624.
[15] T. Kuila, S. Bose, A.K. Mishra, P. Khanra, N.H. Kim, J.H. Lee, Chemical functionalization of graphene and its applications, Prog. Mater. Sci., 57 (2012) 1061–1105.
[16] W.D. Oh, Z. Dong, T. Lim, Generation of sulfate radical through heterogeneous catalysis for organic contaminants removal: current development, challenges and prospects, Appl. Catal., B, 194 (2016) 169–201.
[17] X. Duan, H. Sun, Z. Ao, L. Zhou, G. Wang, S. Wang, Unveiling the active site of graphene-catalyzed peroxymonosulfate activation, Carbon, 107 (2016) 7–15.
[18] L. Tang, Y. Liu, J. Wang, G. Zeng, Y. Deng, H. Dong, H. Feng, J. Wang, B. Peng, Enhanced activation process of persulfate by mesoporous carbon for degradation of aqueous organic pollutants electron transfer mechanism, Appl. Catal., B, 231 (2018) 1–10.
[19] X. Duan, H. Sun, Z. Shao, S. Wang, Nonradical reactions in environmental remediation processes: Uncertainty and challenges, Appl. Catal., B, 224 (2018) 973–982.
[20] S. Wang, L. Xu, J. Wang, Nitrogen-doped graphene as peroxymonosulfate activator and electron transfer mediator for the enhanced degradation of sulfamethoxazole, Chem. Eng. J., 375 (2019) 122041, doi: 10.1016/j.cej.2019.122041.
[21] Y. Zhao, G. Wang, L. Li, X. Dong, X. Zhang, Enhanced activation of peroxymonosulfate by nitrogen-doped graphene/TiO_2 under photo-assistance for organic pollutants degradation: insight into N doping mechanism, Chemosphere, 244 (2020) 125526, doi: 10.1016/j.chemosphere.2019.125526.
[22] P.A. Denis, R. Faccio, A.W. Mombru, Is it possible to dope single-walled carbon nanotubes and graphene with sulfur, ChemPhysChem, 10 (2010) 715–722.
[23] L. Zhang, J. Niu, M. Li, Z. Xia, Catalytic mechanisms of sulfur-doped graphene as efficient oxygen reduction reaction catalysts for fuel cells, J. Phys. Chem. C, 118 (2014) 3545–3553.
[24] J. Zhao, Y. Liu, X. Quan, S. Chen, H. Zhao, H. Yu, Nitrogen and sulfur co-doped graphene/carbon nanotube as metal-free electrocatalyst for oxygen evolution reaction: the enhanced performance by sulfur doping, Electrochim. Acta, 204 (2016) 169–175.
[25] X. Duan, H. Sun, Z. Shao, S. Wang, Nonradical reactions in environmental remediation processes: uncertainty and challenges, Appl. Catal., B, 224 (2018) 973–982.
[26] P. Sun, H. Liu, M. Feng, L. Guo, Z. Zhai, Y. Fang, X. Zhang, V.K. Sharma, Nitrogen-sulfur co-doped industrial graphene as an efficient peroxymonosulfate activator: singlet oxygen-dominated catalytic degradation of organic contaminants, Appl. Catal., B, 251 (2019) 335–345.
[27] A.S. Siddiqui, A. Hayat, M.H. Nawaz, M.A. Ahmad, M. Nasir, Effect of sulfur doping on graphene oxide towards amplified fluorescence quenching based ultrasensitive detection of hydrogen peroxide, Appl. Surf. Sci., 509 (2019) 144695, doi: 10.1016/j.apsusc.2019.144695.
[28] R. Ji, Y. Wu, Y. Bian, Y. Song, H. Cheng, Nitrogen-doped porous biochar derived from marine algae for efficient solid-phase microextraction of chlorobenzenes from aqueous solution, J. Hazard. Mater., 407 (2020) 124785, doi: 10.1016/j.jhazmat.2020.124785.
[29] B. Pna, B. Nka, A. Mr, A. Br, Highly improving the mechanical-responses/thermal-stability of the epoxy nano-composite using novel highly-oxidized multi-walled carbon nanotubes (OMWCNT) functionalized by Zinc-doped Polyaniline (PANI) nanofibers, J. Taiwan Inst. Chem. Eng., 119 (2021) 245–258.
[30] Q. Xu, L. Wang, C. Li, X. Wang, C. Li, Y. Geng, Study on improvement of the proton conductivity and anti-fouling of proton exchange membrane by doping SGO@SiO_2 in microbial fuel cell applications, Int. J. Hydrogen Energy, 44 (2019) 15322–15332.
[31] M.A. Mostafavi, A. Mouradzadegun, Reinforced polymeric nanocomposites of the Amino-Decorated Polycalix[4] resorcinarene with graphene oxide and reduced graphene oxide as promising candidates in materials science, Mater. Sci. Eng. B, 271 (2021) 115273, doi: 10.1016/j.mseb.2021.115273.
[32] N. Wang, B. Lu, L. Li, W. Niu, S. Chen, Graphitic N is responsible for oxygen electroreduction on N-Doped carbons in alkaline electrolytes: insights from activity attenuation studies and theoretical calculations, ACS Catal., 8 (2018) 6827–6836.
[33] X. Du, M.A. Oturan, M. Zhou, N. Belkessa, P. Su, J. Cai, C. Trellu, E. Mousset, Nanostructured electrodes for electrocatalytic advanced oxidation processes: from materials preparation to mechanisms understanding and wastewater treatment applications, Appl. Catal., B, 296 (2021) 120332, doi: 10.1016/j.apcatb.2021.120332.
[34] Q. Zhang, W. Huang, Y. Yu, Y. Zhou, J. Hong, Catalytic performance and mechanism of graphene electrode doped with S and N heteroatoms for N-(4-hydroxyphenyl)ethanamide electrochemical degradation, J. Hazard. Mater., 368 (2019) 316–325.
[35] W. Li, Z. Wang, H. Liao, X. Liu, L. Zhou, Y. Lan, J. Zhang, Enhanced degradation of 2,4,6-trichlorophenol by activated peroxymonosulfate with sulfur doped copper manganese bimetallic oxides, Chem. Eng. J., 3–4 (2020) 128121, doi: 10.1016/j.cej.2020.128121.
[36] J. Hu, H. Dong, J. Qu, Z. Qiang, Enhanced degradation of iopamidol by peroxymonosulfate catalyzed by two pipe corrosion products (CuO and δ-MnO_2), Water Res., 112 (2017) 1–8.
[37] N. Tian, X. Tian, Y. Nie, C. Yang, Z. Zhou, Y. Li, Biogenic manganese oxide: an efficient peroxymonosulfate activation catalyst for tetracycline and phenol degradation in water, Chem. Eng. J., 352 (2018) 469–476.

[38] J. Deng, S.F. Feng, X. Ma, C. Tan, H. Wang, S. Zhou, T. Zhang, J. Li, Heterogeneous degradation of Orange II with peroxymonosulfate activated by ordered mesoporous $MnFe_2O_4$, Sep. Purif. Technol., 167 (2016) 181–189.
[39] M. Lucas, J. Peres, Degradation of the azo dye Reactive Black 5 by Fenton and photo-Fenton oxidation, Dyes Pigm., 71 (2006) 236–244.
[40] H. Zhou, J. Peng, J. Li, J. You, L. Lai, R. Liu, Z. Ao, G. Yao, B. Lai, Metal-free black-red phosphorus as an efficient heterogeneous reductant to boost Fe^{3+}/Fe^{2+} cycle for peroxymonosulfate activation, Water Res., 118 (2021) 116529, doi: 10.1016/j.watres.2020.116529.
[41] S. Yang, Y. Xin, X. Shao, R. Niu, L. Wang, Activated carbon catalyzed persulfate oxidation of Azo dye acid orange 7 at ambient temperature, J. Hazard. Mater., 186 (2011) 659–666.
[42] S. Chen, T.-f. Hu, Q. Zhang, J.-m. Hong, UV–annealing synthesis of sulfur-doped graphene for bisphenol A electrocatalytic degradation, Appl. Surf. Sci., 569 (2021) 151042, doi: 10.1016/j.apsusc.2021.151042.
[43] X. Xu, Y. Yang, Y. Jia, X. Lian, Y. Zhang, F. Feng, Q. Liu, B. Xi, Y. Jiang, Heterogeneous catalytic degradation of 2,4-dinitrotoluene by the combined persulfate and hydrogen peroxide activated by the as-synthesized Fe-Mn binary oxides, Chem. Eng. J., 374 (2019) 776–786.
[44] N. Saeidi, M.D. Esrafili, J.J. Sardroodi, NO electrochemical reduction over $Si\text{-}N_4$ embedded graphene: a DFT investigation, Appl. Surf. Sci., 544 (2020) 148869, doi: 10.1016/j.apsusc.2020.148869.
[45] M.D. Esrafili, B. Nejadebrahimi, Theoretical insights into hydrogenation of CO_2 to formic acid over a single Co atom incorporated nitrogen-doped graphene: a DFT study, Appl. Surf. Sci., 475 (2019) 363–371.